

# A Hybrid Ensemble Learning Approach to Star-galaxy Classification

Edward J. Kim<sup>\*1</sup>, Robert J. Brunner<sup>2</sup>, and Matias Carrasco Kind<sup>3</sup>

<sup>1</sup>*Department of Physics, University of Illinois, Urbana, IL 61801 USA*

<sup>2</sup>*Department of Astronomy, University of Illinois, Urbana, IL 61801 USA*

<sup>3</sup>*National Center for Supercomputing Applications, Urbana, IL 61801 USA*

15 April 2015

## ABSTRACT

Star-galaxy separation in currently ongoing and future large photometric surveys, such as DES and LSST, will detect a vast number of unresolved galaxies at faint magnitudes. There exist a variety of star-galaxy classification techniques, each with their own strengths and weaknesses. In this paper, we present a novel hybrid, ensemble classification framework that combines and fully exploits different techniques to produce a more robust classification. To demonstrate this hybrid technique, we combine a purely morphological classifier, a supervised machine learning technique based on random forest, an unsupervised method based on self-organizing maps, and a hierarchical Bayesian template fitting algorithm. Any of these four methods could easily be replaced by a similar method or be extended to include other existing techniques. Testing with CFHTLenS data, we demonstrate that our combination technique improves the overall performance over any individual classification method.

**Key words:** keywords

## 1 INTRODUCTION

The problem of star-galaxy classification is fundamental to astronomy and goes as far back as Messier (1781). A variety of different strategies have been developed to tackle this long-standing problem, and yet it remains an unsolved challenge. The most commonly used method to classify stars and galaxies in large sky surveys is the morphological separation (Sebok 1979; Kron 1980; Valdes 1982; Yee 1991; Vasconcellos et al. 2011; Henrion et al. 2011). It relies on the assumption that stars appear as point sources while galaxies appear as resolved sources. However, currently ongoing and upcoming large photometric surveys, such as the Dark Energy Survey (DES<sup>1</sup>) and the Large Synoptic Survey Telescope (LSST<sup>2</sup>), will detect a vast number of unresolved galaxies at faint magnitudes. Near a survey’s limit, the photometric observations cannot reliably separate stars from unresolved galaxies by morphology alone without leading to incompleteness and contamination in the star and galaxy samples.

The contamination of unresolved galaxies can be mitigated by using training based algorithms. Machine learning methods have the advantage that it is easier to include extra information, such as concentration indices, shape information, or different model magnitudes. However, they are only reliable within the limits of the training data, and it can be difficult to

extrapolate these algorithms outside the parameter range of the training data. These techniques can be further categorized into supervised and unsupervised learning approaches.

In supervised learning, the input attributes (e.g., magnitudes or colors) are provided along with the truth labels (e.g., star or galaxy). Odewahn et al. (1992) pioneered the application of neural networks to the star-galaxy classification problem, and it has become a core part of the astronomical image processing software SExtractor (Bertin & Arnouts 1996). Other successfully implemented examples include decision trees (Weir et al. 1995; Suchkov et al. 2005; Ball et al. 2006) and Support Vector Machines (Fadely et al. 2012). Unsupervised machine learning techniques are less common as they do not utilize the truth labels during the training process and only the input attributes are used.

Physically based template fitting methods have also been used for the star-galaxy classification problem (Robin et al. 2007; Fadely et al. 2012). Template fitting approaches infer a source’s properties by finding the best match between the measured set of magnitudes (or colors) and the synthetic set of magnitudes (or colors) computed from a set of spectral templates. Although it is not necessary to obtain a high-quality spectroscopic training sample, these techniques do require a representative sample of theoretical or empirical templates that span the possible spectral energy distributions (SEDs) of stars and galaxies. Furthermore, they are not exempt from uncertainties due to measurement errors on the filter response curves, or from mismatches between the observed magnitudes and the template SEDs.

\* jkim575@illinois.edu

<sup>1</sup> <http://www.darkenergysurvey.org/>

<sup>2</sup> <http://www.lsst.org/lsst/>

In this paper, we present a novel star-galaxy classification framework that combines and fully exploits different classification techniques to produce a more robust classification. In particular, we show that the combination of a morphological separation method, a template fitting technique, a supervised machine learning method, and an unsupervised machine learning algorithm can improve the overall performance over any individual method. In Section 2, we describe each of the star-galaxy classification methods. In Section 3, we describe different classification combination techniques. In Section 4, we describe the Canada-France Hawaii Telescope Lensing Survey (CFHTLenS) data set with which we test the algorithms. In Section 5, we compare the performance of our combination techniques to the performance of the individual classification techniques.

## 2 CLASSIFICATION METHODS

In this section, we present four distinct star-galaxy classification techniques. The first method is a supervised machine learning technique named TPC (Trees for Probabilistic Classification), which uses prediction trees and a random forest (Carrasco Kind & Brunner 2013). The second method is an unsupervised machine learning technique named SOMc, which uses self-organizing maps (SOM) and a random atlas to provide a classification citepcarrascokind2014somz. The third method is a Hierarchical Bayesian template fitting technique based on the work by Fadely et al. (2012), which fits SED templates from star and galaxy libraries to an observed set of measured flux values. The fourth method is a morphological separation method, which uses a hard cut in the half-light radius vs. magnitude plane.

Collectively, these four methods represent the majority of all standard star-galaxy classification approaches published in the literature. It is very likely that any new classification technique would be functionally similar to one of these four methods. Therefore, any of these four methods could in principle be replaced by a similar method.

### 2.1 Morphological Separation

The simplest and perhaps the most widely used approach to star-galaxy classification is to make a hard cut in the space of photometric attributes. As a first-order morphological selection of point sources, we adopt a technique that is popular among the weak lensing community (Kaiser et al. 1995). As Figure 1 shows, there is a distinct locus produced by point sources in the half-light radius ( $r_h$ ; estimated by SEXTRACTOR’s FLUX\_RADIUS parameter) vs. the  $i$ -band magnitude plane. A rectangular cut in this size-magnitude plane separates point sources, which are presumed to be stars, from resolved sources, which are presumed to be galaxies. The boundaries of the selection box are determined by manually inspecting the size-magnitude diagram.

One of the disadvantages of such cut-based methods is that it classifies every source with absolute certainty. It is difficult to justify such a decisive classification near a survey’s magnitude limits, where measurement uncertainties generally increase. A more informative approach is to provide probabilistic classifications. Although a recent work by Henrion et al. (2011) implemented a probabilistic classification using a Bayesian approach on the morphological measurements alone,

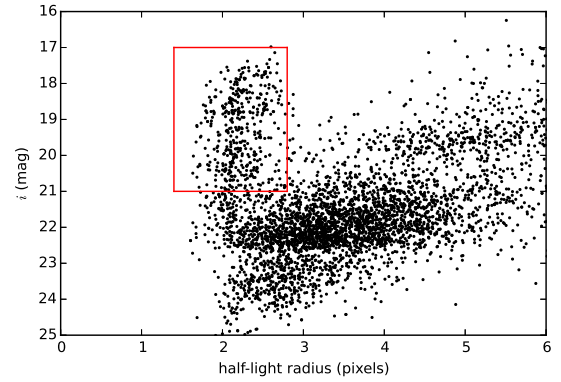


**Figure 1.** Half-light radius ( $r_h$ ) vs. magnitude.

here we use a cut-based morphological separation to demonstrate the advantages of our combination techniques. In particular, we later show that the binary output (i.e., 0 or 1) of cut-based methods can be transformed into a probability estimate by combining them with the probability outputs from other probabilistic classification techniques, such as TPC, SOMc, and HB.

### 2.2 Supervised Machine Learning: TPC

TPC is a parallel, supervised machine learning algorithm that uses prediction trees and random forest techniques (Breiman et al. 1984; Breiman 2001) to produce star-galaxy classification. TPC is a part of a publicly available software package called MLZ<sup>3</sup> (Machine Learning for Photo- $z$ ). The full software package includes, among other capabilities, TPZ, a supervised photo- $z$  technique (regression mode; Carrasco Kind & Brunner 2013), TPC, a supervised star-galaxy classification technique (classification mode), SOMz, an unsupervised photo- $z$  technique (regression mode; Carrasco Kind & Brunner 2014b), and SOMc, an unsupervised star-galaxy classification technique (classification mode).

TPC uses classification trees, a type of prediction trees that are designed to provide a classification or predict a discrete category. Prediction trees are built by asking a sequence of questions that recursively split the data into branches until a terminal leaf is created that meets a stopping criterion (e.g., a minimum leaf size). The optimal split dimension is decided by choosing the attribute that maximizes the *Information Gain* ( $I_G$ ), which is defined as

$$I_G(D_{\text{node}}, X) = I_d(D_{\text{node}}) - \sum_{x \in \text{values}(X)} \frac{|D_{\text{node},x}|}{|D_{\text{node}}|} I_d(D_{\text{node},x}), \quad (1)$$

where  $D_{\text{node}}$  is the training data in a given node,  $X$  is one of the possible dimensions (e.g., magnitudes or colors) along which the node is split, and  $x$  are the possible values of a specific dimension  $X$ .  $|D_{\text{node}}|$  and  $|D_{\text{node},x}|$  are the size of the total training data and the number of objects in a given subset  $x$  within the current node, respectively.  $I_d$  is the impurity degree index, and TPC can calculate  $I_d$  from any of the three standard different impurity indices: *information entropy*, *Gini*

<sup>3</sup> <http://lcdm.astro.illinois.edu/code/mlz.html>

impurity, and classification error. Here, we use the information entropy, which is defined similarly to the thermodynamic entropy:

$$I_d(D) = -f_g \log_2 f_g - (1 - f_g) \log_2 f_g, \quad (2)$$

where  $f_g$  is the fraction of galaxies in the training data. At each node in our tree, we scan all dimensions to identify the split point that maximizes the information gain as defined by Equation 1, and select the attribute that maximizes the impurity index overall.

In a technique called random forest, we create bootstrap samples (i.e.,  $N$  randomly selected objects with replacement) from the input training data by sampling repeatedly from the magnitudes using the magnitude errors. We use these bootstrap samples to construct multiple, uncorrelated prediction trees whose individual predictions are aggregated to produce a star-galaxy classification for each source.

We also use a cross validation technique called Out-of-Bag (OOB; Breiman et al. 1984; Carrasco Kind & Brunner 2013). When a tree (or a map) is built in TPC (or SOMc), a fraction of the training data, usually one-third, is left out and not used in training the trees or maps. After a tree is constructed using two-thirds of the training data, the final tree is applied to the remaining one-third to make a classification. This process is repeated for every tree, and the predictions from each tree are aggregated for each object to make the final star-galaxy classification. We emphasize that if an object is used for training a given tree, it is never used for subsequent prediction by that tree. Thus, the OOB data is an unbiased estimation of the errors and can be used as cross-validation data as long as the OOB data remain similar to the final test data set. The OOB technique can also provide extra information such as a ranking of the relative importance of the input attributes used in the prediction. The OOB technique can prove extremely valuable when calibrating the algorithm, when deciding which attributes to incorporate in the construction of the trees, and when combining this approach with other techniques.

### 2.3 Unsupervised Machine Learning: SOMc

A Self-Organizing Map (SOM; Kohonen 1990, 2001) is an unsupervised, artificial neural network algorithm that is capable of projecting high-dimensional input data onto a low-dimensional map through a process of competitive learning. In astronomical applications, the high-dimensional input data can be magnitudes, colors, or some other photometric attributes. The output map is usually chosen to be two-dimensional for the visualization. The differences between a SOM and other neural network algorithms are that a SOM is unsupervised, there are no hidden layers and therefore no extra parameters, and it produces a direct mapping between the training set and the output network. In fact, a SOM can be viewed as a non-linear generalization of a principal component analysis (PCA) algorithm.

The key characteristic of SOM is that it retains the topology of the input training set, revealing correlations between input data that are not obvious. The method is unsupervised: the user is not required to specify the desired output during the creation of the lower-dimensional map, and the mapping of the components from the input vectors is a natural outcome of the competitive learning process.

During the construction of a SOM, each node on the two-dimensional map is represented by weight vectors of the same dimension as the number of attributes used to create the map itself. In an iterative process, each object in the input sample is individually used to correct these weight vectors. This correction is determined so that the specific neuron (or node), which at a given moment best represents the input source, is modified along with the weight vectors of that node's neighboring neurons. As a result, this sector within the map becomes a better representation of the current input object. This process is repeated for every object in the training data, and the entire process is repeated for several iterations. Eventually, the SOM converges to its final form where the training data is separated into groups of similar features.

In a similar approach to random forest in TPZ and TPC, SOMz uses a technique called *random atlas* to provide photo- $z$  estimation (Carrasco Kind & Brunner 2014b). In random atlas, the prediction trees of random forest are replaced by maps, and each map is constructed from different bootstrap samples of the training data. Furthermore, we create random realizations of the training data by perturbing the input attributes by their measurement error. For each map, we can either use all available attributes, or randomly select a subsample of the attribute space. This SOM implementation can also be applied to the classification problem, and we refer to it as SOMc in order to differentiate it from the photo- $z$  estimation problem (regression mode). We also use the random atlas approach in some of the classification combination approaches as discussed in Section 3.

One of the most important parameter in SOMc is the topology of the two-dimensional SOM, which can be rectangular, hexagonal, or spherical. To classify stars and galaxies in the CFHTLenS data, we use a spherical topology, which is constructed by using HEALPIX (Górski et al. 2005). Furthermore, similar to TPC, we use the OOB technique to make an unbiased estimation of errors. For a complete description of the SOM implementation and its application to the estimation of photo- $z$  probability distribution functions, we refer the reader to Carrasco Kind & Brunner (2014b).

### 2.4 Template fitting: Hierarchical Bayesian

One of the most common methods to classify a source based on its observed magnitudes is template fitting. Template fitting algorithms do not require a spectroscopic training sample; there is no need for additional knowledge outside the observed data and the template SEDs. However, any incompleteness in our knowledge of the template SEDs that fully span the possible SEDs of observed sources may lead to misclassification of sources.

Bayesian algorithms use Bayesian inference to quantify the relative probability that each template matches the input photometry and determines a probability estimate by computing the posterior that a source is a star or a galaxy. In this work, we have modified and parallelized a publicly available Hierarchical Bayesian (HB) template fitting algorithm by Fadely et al. (2012). In this section, we provide a brief description of the HB template fitting technique; for the details of the underlying HB approach, we refer the reader to Fadely et al. (2012).

We write the posterior probability that a source is a star as

$$P(S|\mathbf{x}, \theta) = P(\mathbf{x}|S, \theta) P(S|\theta), \quad (3)$$

where  $\mathbf{x}$  represents a given set of observed magnitudes. We have also introduced the *hyperparameter*  $\theta$ , a nuisance parameter that characterizes our uncertainty in the prior distribution. To compute the likelihood that a source is a star, we marginalize over all star and galaxy templates  $\mathbf{T}$ . In a template-fitting approach, we marginalize by summing up the likelihood that a source has the set of magnitudes  $\mathbf{x}$  for a given star template as well as the likelihood for a given galaxy template:

$$P(\mathbf{x}|S, \theta) = \sum_{t \in \mathbf{T}} P(\mathbf{x}|S, t, \theta) P(t|S, \theta). \quad (4)$$

The likelihood of each template  $P(\mathbf{x}|S, \theta)$  is itself marginalized over the uncertainty in the template-fitting coefficient. Furthermore, for galaxy templates, we introduce another step that marginalizes the likelihood by redshifting a given galaxy template by a factor of  $1 + z$ .

Marginalization in Equation 4 requires that we specify the prior probability  $P(t|S, \theta)$  that a source has spectral template  $t$  (at a given redshift). Thus, the probability that a source is a star (or a galaxy) is either the posterior probability itself if a prior is used, or the likelihood itself if an uninformative prior is used. In a Bayesian analysis, it is preferable to use a prior, which can be directly computed either from physical assumptions, from an empirical function calibrated by using a spectroscopic training sample, or from an empirical function calibrated by using machine learning techniques. In an HB approach, the entire sample of sources is used to infer the prior probabilities for each individual source.

Since the templates are discrete in both SED shape and physical properties, we parametrize the prior probability of each template as a discrete set of weights such that

$$\sum_{t \in \mathbf{T}} P(t|S, \theta) = 1. \quad (5)$$

These weights correspond to the hyperparameters, which can be inferred by sampling the posterior probability distribution in the hyperparameter space. For the sampling, we use **emcee**, a Python implementation of the affine-invariant Markov Chain Monte Carlo (MCMC) ensemble sampler (Foreman-Mackey et al. 2013).

As the goal of template fitting methods is to minimize the difference between observed and theoretical magnitudes, this approach heavily relies on both the use of SED templates and the accuracy of the transmission functions for the filters used for particular survey. For our stellar templates, we use the empirical SED library from Pickles (1998). The Pickles library consists of 131 stellar templates, which span all normal spectral types and luminosity classes at solar abundance, as well as metal-poor and metal-rich F-K dwarf and G-K giant and supergiant stars. [We supplement the stellar library with 100 SEDs from Chabrier et al. \(2000\), which include low mass stars and brown dwarfs with different  \$T\_{\text{eff}}\$  and surface gravities. We also include four white dwarf templates of Bohlin et al. \(1995\).](#) For our galaxy templates, we use the four CWW spectra from Coleman et al. (1980), which include an Elliptical, an Sba, an Sbb, and an Irregular galaxy template. When extending an analysis to higher redshift, the CWW library is often augmented with two star bursting galaxy templates from Kinney et al. (1996). [From the six original CWW and Kinney](#)

[spectra, intermediate templates are created by interpolation for a total of 51 SEDs.](#)

All of the above templates are convolved with the filter response curves to generate model magnitudes. These response curves consist of  $u, g, r, i, z$  filter transmission functions for the observations taken by the Canada-France Hawaii Telescope (CFHT).

### 3 CLASSIFICATION COMBINATION METHODS

Building on the work in the field of ensemble learning, we combine the predictions from individual star-galaxy classification techniques using ensemble learning techniques known as Bayesian Model Combination (BMC) and a variant of an ensemble learning technique known as stacking. The main idea behind ensemble learning is to weigh the predictions from individual models and combine them to obtain a prediction that outperforms every one of them individually (Rokach 2010).

#### 3.1 Unsupervised Binning

Given the variety of star-galaxy classification methods we are using, we fully expect the relative performance of the individual techniques to vary across the parameter space spanned by the data. For example, it is reasonable to expect supervised techniques to outperform other techniques in areas of parameter space that are well-populated with training data. Similarly, we can expect unsupervised approaches such as SOM or template fitting approaches to generally perform better when training data is either sparse or unavailable.

We therefore adopt the binning strategy similar to Carrasco Kind & Brunner (2014a). In this binning strategy, we allow different classifier combinations in different parts of parameter space by creating two-dimensional SOM representations of the full nine-dimensional magnitude-color space:  $u, g, r, i, z, u - g, g - r, r - i, \text{ and } i - z$ . A SOM representation can be rectangular, hexagonal, or spherical; here we choose a  $10 \times 10$  rectangular topology to facilitate visualization as shown in Figure. 2. For all combination methods, we use only the OOB (cross validation) data contained in each cell to compute the relative weights for the base classifiers. The weights within individual cells are then applied to the test data to make the prediction.

Furthermore, we construct a collection of SOM representations and subsequently combine the predictions from each map into a meta-prediction. Given a training sample of  $N$  sources, we generate  $N_R$  random realizations of training data by perturbing the attributes with the measured uncertainty for each attribute. The uncertainties are assumed to be normally distributed. In this manner, we reduce the bias towards the data and introduce randomness in a systematic manner. For each random realization of a training sample, we create  $N_M$  bootstrap samples of size  $N$  to generate  $N_M$  different maps.

After all maps are built, we have a total of  $N_R \times N_M$  probabilistic outputs for each of the  $N$  sources. To produce a single probability estimate for each source, one can take the mean, the median, or some other simple statistic. With a sufficient number of maps, we find that there is usually negligible difference between taking the mean and taking the median, and so we use the median in the following sections. We note that it is also possible to establish confidence intervals using the distribution of the probability estimates.

### 3.2 Weighted Average

The simplest approach to combine different combination techniques is to simply add the individual classifications from the base classifiers and renormalize the sum. In this case, the final probability is given by

$$P(S|\mathbf{x}, \mathbf{M}) = \sum_i P(S|\mathbf{x}, M_i), \quad (6)$$

where  $\mathbf{M}$  is the set of models (TPC, SOMc, HB, and morphological separation in our work). We improve on this simple approach by using the binning strategy to calculate the weighted average of each bin separately, rather than globally.

### 3.3 Bucket of Models (BoM)

After the multi-dimensional input data have been binned, we can use the cross-validation data to choose the best model within each bin, and we use only that model within that specific bin to make predictions for the test data. We use the mean squared error (MSE; also known as Brier score (Brier 1950)) as a classification error metric. We define MSE as

$$\text{MSE} = \frac{1}{N} \sum_{i=0}^{N-1} (y_i - \hat{y}_i)^2, \quad (7)$$

where  $\hat{y}_i$  is the actual truth value (e.g., 0 or 1) of the  $i^{\text{th}}$  data, and  $y_i$  is the probability prediction made by the models. Thus, a model with the minimum MSE is chosen in each bin and is assigned a weight of one, and zero for all other models. However, the chosen model is allowed to vary between different bins.

### 3.4 Stacking

Instead of selecting a single model that performs best within each bin, we can train a learning algorithm to combine the output values of several other base classifiers in each bin. An ensemble learning method of using a meta-classifier to combine lower-level classifiers is known as *stacking* or *stacked generalization* (Wolpert 1992). Although any arbitrary algorithm can theoretically be used as a meta-classifier, a logistic regression or a linear regression is often used in practice. In our work, we use a single-layer multi-response linear regression algorithm, which often shows the best performance (Breiman 1996; Ting & Witten 1999).

### 3.5 Bayesian Model Combination

We also use a model combination technique (Monteith et al. 2011) known as Bayesian Model Combination (BMC). BMC uses Bayesian principles to generate an ensemble combination of different classifiers (Monteith et al. 2011). The posterior probability that a source is a star is given by

$$P(S|\mathbf{x}, \mathbf{D}, \mathbf{M}, \mathbf{E}) = \sum_{e \in \mathbf{E}} P(S|\mathbf{x}, \mathbf{M}, e) P(e|\mathbf{D}), \quad (8)$$

where  $\mathbf{D}$  is the data set, and  $e$  is an element in the ensemble space  $\mathbf{E}$  of possible model combinations. By Bayes' Theorem, the posterior probability of  $e$  given  $\mathbf{D}$  is given by

$$P(e|\mathbf{D}) = \frac{P(e)}{P(\mathbf{D})} \prod_{d \in \mathbf{D}} P(d|e) \propto P(e) \prod_{d \in \mathbf{D}} P(d|e). \quad (9)$$

Here, the product of  $P(d|e)$  is over all individual data  $d$  in the training data  $\mathbf{D}$ , and  $P(\mathbf{D})$  is merely a normalization factor and not important.

For binary classifiers whose output is either zero or one (e.g., a cut-based morphological separation), we assume that each example is corrupted with an average error rate  $\epsilon$ . This means that  $P(d|e) = 1 - \epsilon$  if the combination  $e$  correctly predicts class  $\hat{y}_i$  for the  $i^{\text{th}}$  object, and  $P(d|e) = \epsilon$  if it predicts an incorrect class. The average rate  $\epsilon$  can be estimated by the fraction  $(M_g + M_s)/N$ , where  $M_g$  is the number of true galaxies classified as stars,  $M_s$  is the number of true stars classified as galaxies, and  $N$  is the total number of sources. Equation 9 then becomes

$$P(e|\mathbf{D}) \propto P(e) (1 - \epsilon)^{N_s + N_g} (\epsilon)^{M_s + M_g}. \quad (10)$$

For probabilistic classifiers, we can directly use the probabilistic predictions and write Equation 9 as

$$P(e|\mathbf{D}) \propto P(e) \prod_{i=0}^{N-1} \hat{y}_i y_i + (1 - \hat{y}_i)(1 - y_i). \quad (11)$$

Although the space  $\mathbf{E}$  of potential model combinations is in principle infinite, we can produce a reasonable finite set of potential model combinations by using sampling techniques. In our implementation, the weights of each combination of the base classifiers is obtained by sampling from a Dirichlet distribution. We first set all alpha values of a Dirichlet distribution. We then sample this distribution  $q$  times to obtain  $q$  sets of weights. For each combination, we assume a uniform prior and calculate  $P(e|\mathbf{D})$  using Equation 9. We select the combination with the highest  $P(e|\mathbf{D})$ , and update the alpha values by adding the weights of the most probable combination to the current alpha values. The next  $q$  weight sets of weights are drawn using the updated alpha values.

We continue the sampling process until we reach a predefined number of combinations, and finally use Equation 8 to compute the posterior probability that a source is a star (or a galaxy). In this paper, we use a  $q$  value of three, and 1,000 model combinations were considered.

We also use a binned version of the BMC technique, where we use a SOM representation to apply different model combinations for different regions of the parameter space. We however note that introducing randomness through the construction of different SOM representations does not show significant improvement over using only one single SOM representation. This similarity is likely due to the randomness that has already been introduced by the sampling from the Dirichlet distribution. Thus, our BMC technique uses one SOM, while other base models (WA, BoM, and stacking) generate  $N_R$  random realizations of  $N_M$  maps.

## 4 DATA

We use photometric data from the Canada-France-Hawaii Telescope Lensing Survey (CFHTLenS<sup>4</sup>; Heymans et al. 2012;

<sup>4</sup> <http://www.cfhtlens.org/>

Erben et al. 2013; Hildebrandt et al. 2012). This catalog consists of more than twenty five million objects with a limiting magnitude of  $i_{AB} \approx 25.5$ . It covers a total of 154 square degrees in the four fields of CFHT Legacy Survey (CFHTLS; Gwyn 2012) observed in the five photometric bands:  $u$ ,  $g$ ,  $r$ ,  $i$ , and  $z$ .

We have cross-matched reliable spectroscopic galaxies from the Deep Extragalactic Evolutionary Probe Phase 2 (DEEP2; Davis et al. 2003; Newman et al. 2013), the Sloan Digital Sky Survey Data Release 10 (Ahn et al. 2014, SDSS-DR10), the Visible imaging Multi-Object Spectrograph (VIMOS) Very Large Telescope (VLT) Deep Survey (VVDS; Le Fèvre et al. 2005; Garilli et al. 2008), and the VIMOS Public Extragalactic Redshift Survey (VIPERS; Garilli et al. 2014). In the end, we have 8,545 stars and 57,843 galaxies available for the training and testing processes.

Our goal here is not to obtain the best classifier performance; for this we would have fine tuned individual base classifiers and chosen sophisticated models best suited to the particular properties of the CFHTLenS data. For example, Hildebrandt et al. (2012) suggest that all objects with  $i > 23$  in the CFHTLenS dataset may be classified as galaxies without significant incompleteness in the galaxy sample. Although this approach works because the high Galactic latitude fields of the CFHTLS contain relatively few stars, it is very unlikely that such an approach will meet the science requirements for the quality of star-galaxy classification in lower latitude, star-crowded fields. Rather, our goal for the CFHTLenS dataset is to demonstrate the usefulness of combining different classifiers even when the base classifiers may be poor or trained on partial data.

## 5 RESULTS AND DISCUSSION

In this section, we present the classification performance of the four different combination techniques, as well as the individual star-galaxy classification techniques on the CFHTLenS test data.

### 5.1 Classification Metrics

Probabilistic classification models can be considered as functions that output a probability estimate of each source to be in one of the classes (e.g., a star or a galaxy). Although the probability estimate can be used as a weight in subsequent analyses to improve or enhance a particular measurement (Ross et al. 2011), it can also be converted into a class label by using a threshold (probability cut). The simplest way to choose the threshold is to set it to a fixed value, e.g.,  $p_{\text{cut}} = 0.5$ . This is, in fact, what is often done (e.g., Henrion et al. 2011; Fadely et al. 2012). However, choosing 0.5 as a threshold is not the best choice for an unbalanced data set, where galaxies outnumber stars. Furthermore, setting a fixed threshold ignores the operating condition (e.g., science requirements, stellar distribution, misclassification costs) where the model will be applied.

When we have no information about the operating condition when evaluating the performance of classifiers, there are effective tools such as the Receiver Operating Characteristic (ROC) curve (Swets et al. 2000). An ROC curve is a graphical plot that illustrates the true positive rate versus the false positive rate of a binary classifier as its classification threshold (probability cut) is varied. The Area Under the Curve (AUC)

**Table 1.** The definition of the classification performance metrics.

Metric	Meaning
AUC	Area under the Receiver Operating Curve
MSE	Mean squared error
$c_g$	Galaxy completeness
$p_g$	Galaxy purity
$c_s$	Star completeness
$p_s$	Star purity
$p_g(c_g = x)$	Galaxy purity at $x$ galaxy purity
$p_s(c_s = x)$	Star purity at $x$ star purity

summarizes the curve information in a single number, and can be used as an assessment of the overall performance.

In astronomical applications, the operating condition usually translates to the completeness and purity requirements of the star/galaxy sample. We define the galaxy *completeness*  $c_g$  (also known as recall or sensitivity) as the fraction of the number of true galaxies classified as galaxies out of the total number of true galaxies,

$$c_g = \frac{N_g}{N_g + M_g}, \quad (12)$$

where  $N_g$  is the number of true galaxies classified as galaxies and  $M_g$  is the number of true galaxies classified as stars. We define the galaxy *purity*  $p_g$  (also known as precision or positive predictive value) as the fraction of the number of true galaxies classified as galaxies out of the total number of objects classified as galaxies,

$$p_g = \frac{N_g}{N_g + M_s}, \quad (13)$$

where  $M_s$  is the number of true stars classified as galaxies. Star completeness and purity are defined in a similar manner.

One of the advantages of a probabilistic classification is that the threshold can be adjusted to produce a more complete but less pure sample, or a less complete but more pure one. To compare the performance of probabilistic classification techniques with that of the morphological separation, which has a fixed completeness ( $c_g = 0.9964$ ,  $c_s = 0.7145$ ) at a certain purity ( $p_g = 0.9484$ ,  $p_s = 0.9666$ ), we adjust the threshold of probabilistic classifiers until the galaxy completeness matches that of the morphological classifier to compute  $p_g$  at  $c_g = 0.9964$ . Similarly, the star purity  $p_s$  at  $c_s = 0.7145$  is computed by adjusting the threshold values until the star completeness of each classifier is equal to that of the morphological classifier.

We can also compare the performance of different classification techniques by assuming an arbitrary operating condition. For example, weak lensing science measurements of the DES require  $c_g > 0.960$  and  $p_g > 0.778$  to control both the statistical and systematic errors on the cosmological parameters, and  $c_s > 0.250$  and  $p_s > 0.970$  for stellar Point Spread Function (PSF) calibration (Soumagnac et al. 2013). Although these values will likely be different for the science cases of the CFHTLenS data, we adopt these values to compare the classification performance at a reasonable operating condition. Thus, we compute  $p_g$  at  $c_g = 0.960$  and  $c_s$  at  $p_s = 0.250$ . We also use the MSE defined in Equation 7 as a classification error metric.

### 5.2 Classifier Combination

We present in Table 2 the classification performance obtained by applying the four different combination techniques, as well



**Table 2.** A summary of the classification performance metrics for the four individual methods and the four different classification combination methods as applied to the CFHTLenS data, with no cut applied to the training data set. The definition of the metrics is summarized in Table 1. The bold entries highlight the best performance values within each column.

Classifier	AUC	MSE	$p_g (c_g = 0.9964)$	$p_s (c_s = 0.7145)$	$p_g (c_g = 0.9600)$	$p_s (c_s = 0.2500)$
TPC	<b>0.9870</b>	0.0208	0.9714	0.9838	0.9918	0.9977
SOMc	0.9683	0.0452	0.9125	0.8454	0.9788	0.9551
HB	0.9403	0.0705	0.9219	0.7017	0.9471	0.6963
Morphology	-	0.0397	0.9597	0.9666	-	-
WA	0.9806	0.0266	0.9755	0.9926	0.9872	0.9977
BoM	0.9870	0.0208	0.9714	0.9838	0.9918	0.9977
Stacking	0.9842	0.0194	0.9752	0.9902	0.9918	1.0000
BMC	0.9852	<b>0.0174</b>	<b>0.9800</b>	<b>0.9959</b>	<b>0.9924</b>	1.0000

as the individual star-galaxy classification techniques, on the CFHTLenS test data. The bold entries highlight the best technique for any particular metric. The first four rows show the performance of four individual star-galaxy classification techniques. Given the wealth of training data, it is not surprising that our supervised machine learning technique TPC outperforms other unsupervised technique. TPC is thus shown in the first row as the benchmark.

The simplest of the combination techniques, WA and BoM, generally do not perform better than TPC. It is also interesting that, even with binning the parameter space and selecting the best model within each bin, BoM almost always chooses TPC as the best model, and therefore gives the same performance as TPC in the end. However, our BMC and stacking techniques have a similar performance and often outperform TPC. Although TPC shows the best performance as measured by the AUC, BMC shows the best performance in all other metrics.

In Figure 2, we show the mean CFHTLenS  $i$ -band magnitude in the top left panel and the fraction of stars in each cell in the top right panel. The bottom two panels show the mean  $u - g$  and  $g - r$  colors. These two-dimensional maps clearly shows the ability of the SOM to preserve relationships between sources when it projects the full nine-dimensional space to the two-dimensional map. The SOM mapping is a non-linear representation of all magnitudes and colors, and thus these SOM maps should only be used to provide guidance.

We can also use the same SOM to determine the relative weights for the four individual classification methods for each cell. We present the four weight maps for the BMC technique in Figure 3. In these maps, a redder color indicates a higher weight, or equivalently that the corresponding weight performs better in that region. These weight maps demonstrate the variation in the performance of the individual techniques across the two-dimensional parameter space defined by the SOM. Not surprisingly, the morphological separation performs best in the top left corner of the  $i$ -band magnitude map, which corresponds to the brightest CFHTLenS magnitudes  $i \lesssim 20$ . On the other hand, TPC seems to perform best in the region that corresponds to intermediate magnitudes  $20 \gtrsim i \gtrsim 22.5$  and  $1.5 < u - g < 3.0$ . Our unsupervised learning method SOMc performs relatively better at fainter magnitudes  $i > 21.5$  with  $0 < u - g < 0.5$  and  $0 < g - r < 0.5$ . Although HB shows the worst performance when there exists ample training data, BMC still utilizes information from HB to produce an overall improvement in performance, especially at intermediate magnitudes  $20 \gtrsim i \gtrsim 22$ .

In Figure 4, we compare the star and galaxy purity values for morphological separation, TPC, and BMC techniques as a function of  $i$ -band magnitude. Although morphological

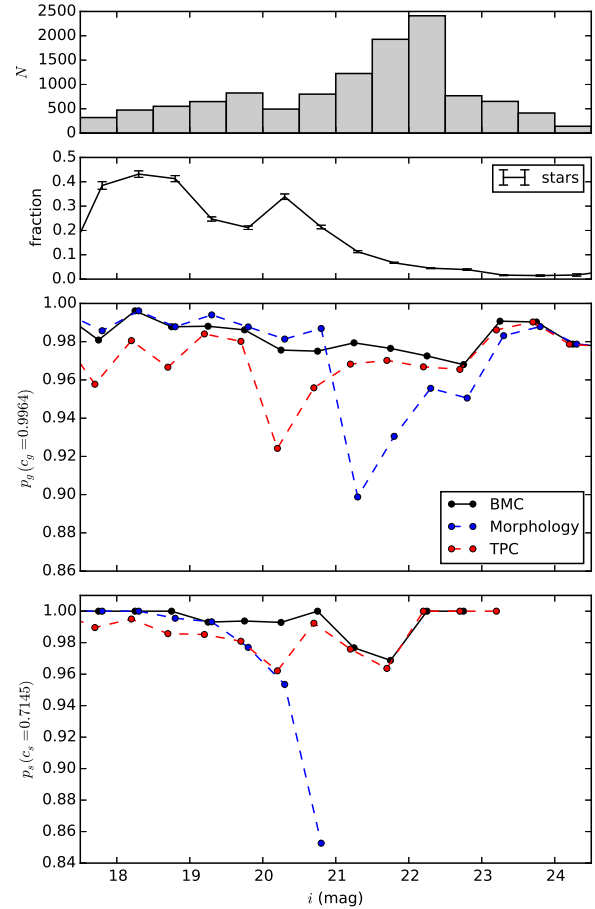


**Figure 4.** Purity of morphological separation, TPC, and BMC techniques as a function of the  $i$ -band magnitude. The top panel shows the histogram of objects in the test data set. The second panel shows the fraction of stars as a function of magnitude. The error bars are Poisson. The bottom two panels compare the galaxy and star purity for morphological separation, TPC, and BMC techniques as a function of magnitude. The error bars for completeness and purity are not shown for clarity, but they are approximately 10 percent.

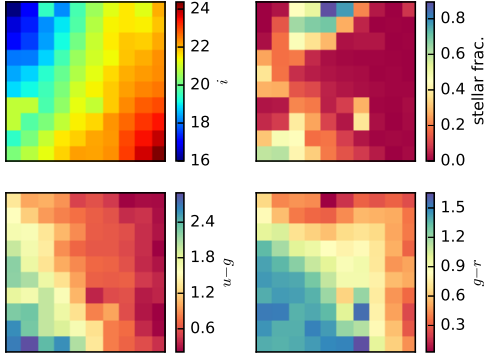


**Figure 2.** A two-dimensional 10×10 SOM representation showing the mean  $i$ -band magnitude (top left), the fraction of true stars in each cell (top right), and the mean values of  $u - g$  and  $g - r$  for the cross validation data.

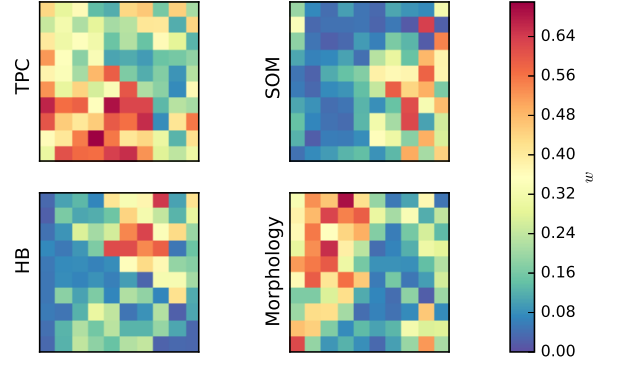


**Figure 3.** A two-dimensional 10×10 SOM representation showing the relative weights for the BMC combination technique applied to the four individual methods for the CFHTLenS data.

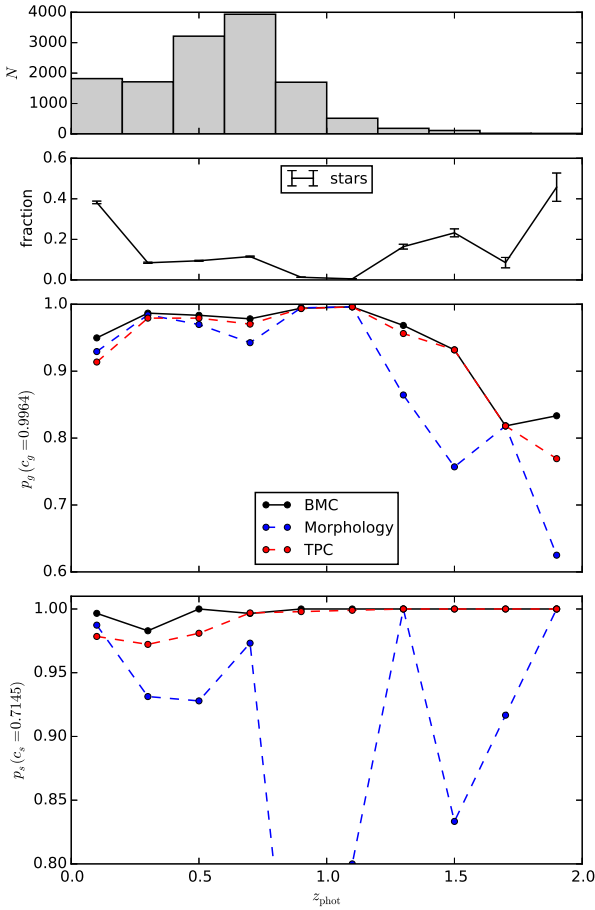


**Figure 5.** The same figures as Figure 4, but as a function of photometric redshift estimate (photo- $z$ ).

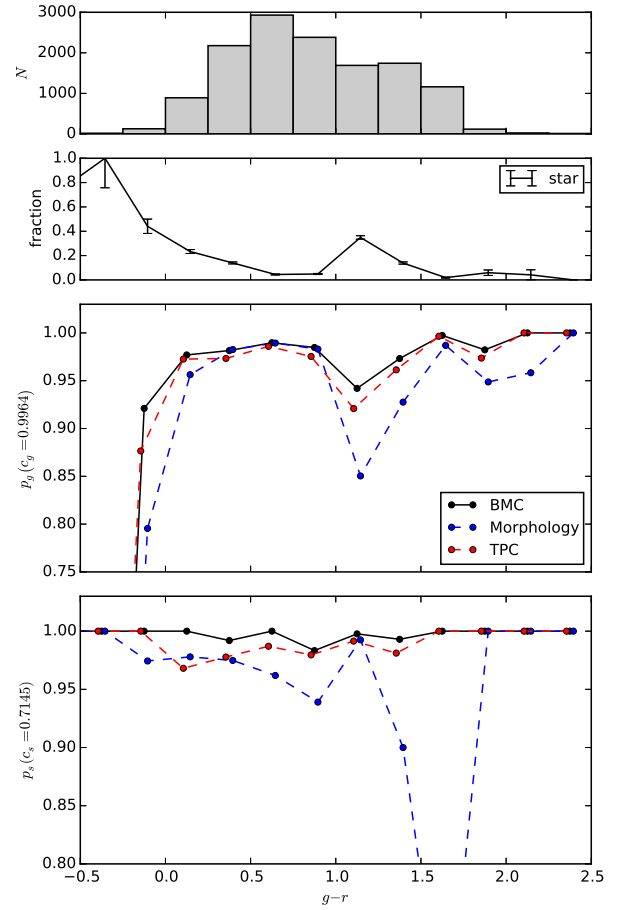


**Figure 6.** The same figure as Figure ??, but as a function of  $g - r$  color.



separation shows a slightly better performance at bright magnitudes  $i < 21$ , BMC outperforms both morphological separation and TPC at faint magnitudes  $i > 21$ . As shown in Figure 4, the histogram of distribution of objects peaks at  $i \sim 22$ , and BMC therefore outperforms the morphological separation technique for the majority of objects. It is also clear that BMC outperforms TPC over all magnitudes. BMC can presumably accomplish this by combining information from all base classifiers, e.g., giving more weight to the morphological separation method at bright magnitudes.

We also show the star and galaxy purity values of Table 2 as a function of photometric redshift in Figure 5. Photo- $z$  is estimated with the BPZ algorithm (Benítez 2000) and provided with the CFHTLenS photometric redshift catalogue (Hildebrandt et al. 2012). Although the morphological separation method outperformed BMC at bright magnitudes in Figure 4, it is clear that BMC outperforms both morphological separation and TPC over all redshift range.

In Figure 6, we present how the star and galaxy purity values vary as a function of  $g - r$  color. It is again clear that BMC outperforms both morphological separation and TPC over all  $g - r$  color range.

### 5.3 Heterogeneous Training

It is very costly in terms of telescope time to obtain a large sample spectroscopic observations down to the limiting magnitude of a photometric sample. Thus, we investigate the impact of training set quality by analyzing in detail a more realistic case where the training data is available only for a small number of objects at bright magnitudes. To emulate this scenario, we only use objects that have spectroscopic labels from the VVDS 0226-04 field (which is located within the CFHTLS W1 field) and impose a magnitude cut of  $i < 22.0$  in the training data, leaving us a training set with 1,365 objects. We apply the same four star-galaxy classification techniques and four different combination methods, and test them on the same test data. Since the demographics of sources in the test data set does not show the same distribution as the training data set, this also serves as a test of the efficacy of heterogenous training data.

We present in Table 3 the same six metrics for each method, and highlight the best method for each metric. Overall, the results obtained for the reduced data set are remarkable. With poor training data, our data-driven methods, TPC and SOMc, suffer a significant decrease in performance, although they still in general perform better than the template fitting algorithm HB. The performance of our morphological separation method does not depend on the training data, and shows the best result in the MSE metric. It also outperforms other base classifiers in galaxy purity at galaxy completeness of 0.9964 and in star purity at star completeness of 0.7145.

Without sufficient training data, the advantage of classification combination techniques is more obvious. Even WA, the simplest of combination techniques, outperforms all individual classification techniques. Interestingly, although TPC does not perform better than morphological separation, BoM still chooses TPC as the best model within each SOM cell and shows exactly the same performance metrics as TPC. Stacking and BMC techniques still outperform all individual classification techniques, and BMC's improvement in performance over TPC or morphological separation is impressive. Overall, the im-

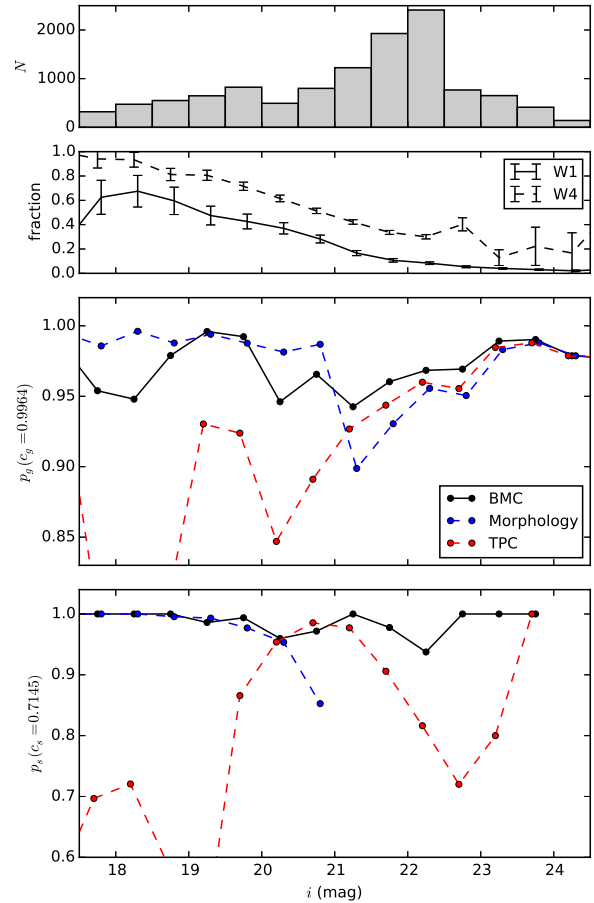


**Figure 9.** Purity as a function of the  $i$ -band magnitude for morphological separation, TPC, and BMC techniques in the VVDS W1 field with  $i < 22$ . We repeat in the top panel shows the histogram of objects in the test data set. The second panel shows the fraction of stars in the VVDS W1 and W4 fields. The error bars are Poisson. The bottom two panels compare the galaxy and star purity for morphological separation, TPC, and BMC techniques as a function of magnitude. The error bars for completeness and purity are not shown for clarity, but they are approximately 10 percent.

provements are small but still significant since these metrics are averaged over the full test data.

In Figure 8, we again show the  $10 \times 10$  two-dimensional weight map defined by the SOM. When the quality of training data is relatively poor, the performance of data driven algorithms will decrease, while the performance of template fitting algorithms such as HB is independent of training data. Thus, comparing the weight maps of Figure 3 and Figure 8, it is perhaps not surprising that BMC algorithm now uses more information from morphological separation and HB, while it uses considerably less information from TPC. It is not surprising that the morphological separation method performs best at bright magnitudes, and BMC assigns more weight to HB at fainter magnitudes.

We present the star and galaxy purity values of Table ??

**Table 3.** A summary of the classification performance metrics for the four individual methods and the four different classification combination methods as applied to the CFHTLenS data in the VVDS W1 field with a magnitude cut of  $i < 22.0$ . The definition of the metrics is summarized in Table 1. The bold entries highlight the best performance values within each column.

Classifier	AUC	MSE	$p_g (c_g = 0.9964)$	$p_s (c_s = 0.7145)$	$p_g (c_g = 0.9600)$	$p_s (c_s = 0.2500)$
TPC	0.9399	0.0511	0.9350	0.7060	0.9570	0.9747
SOMc	0.8861	0.0989	0.8843	0.4316	0.9165	0.6263
HB	0.9386	0.0760	0.9325	0.6911	0.9424	0.6918
Morphology	-	0.0397	0.9597	0.9666	-	-
WA	0.5245	0.3292	0.8719	0.1330	0.8731	0.1457
BoM	0.4988	0.3329	0.8723	0.1265	0.8715	0.1300
Stacking	0.9031	0.0776	0.9605	0.6753	0.9605	0.6753
BMC	<b>0.9738</b>	<b>0.0291</b>	<b>0.9696</b>	<b>0.9862</b>	<b>0.9856</b>	<b>1.0000</b>

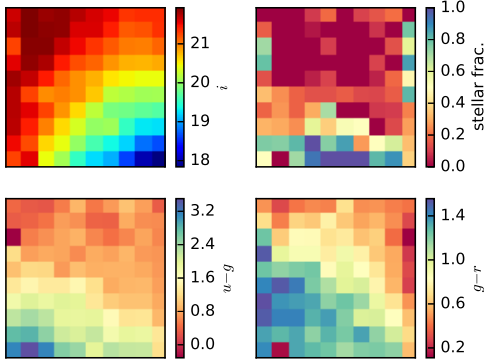


**Figure 7.** The same figure as Figure 2 but for the BMC technique applied to the four individual methods trained with the CFHTLenS data in the VVDS W1 field with  $i < 22$ .

as a function of  $i$ -band magnitude in Figure 9. It is clear that BMC outperforms both morphological separation and TPC classification techniques over all magnitudes. The galaxy purity of BMC is significantly better than that of TPC at bright magnitudes,  $i \lesssim 21.5$ , while they are similar at faint magnitudes. The star purity of BMC shows improvement over that of TPC at faint magnitudes, while they are similar at bright magnitudes. As suggested by the weight maps in Figure 8, BMC can accomplish this by combining information from all base classifiers, e.g., giving more weight to the morphological separation method at bright magnitudes. We can also see in the bottom two panels that the performance of morphological separation suffers at intermediate magnitudes  $21 \lesssim i \lesssim 23$ , while BMC shows consistently better performance over all magnitude ranges.

We also show the star and galaxy purity values of Table ?? as a function of photometric redshift in Figure 5. Photo- $z$  is estimated with the BPZ algorithm (Benítez 2000) and provided with the CFHTLenS photometric redshift catalogue (Hildebrandt et al. 2012). It is again clear that BMC outperforms both individual classification techniques over all redshift range.

We show the distribution of posterior star probabilities in Figures 12 and 13. The histogram of spectroscopic galaxies is in blue, and the histogram of true stars is in red. It is interesting that the BMC technique assigns a probability  $P(S)$  greater than 0.6 to almost no true galaxies in Figure 12, presumably because BMC utilizes information from different types of classification techniques. This pattern is more pro-

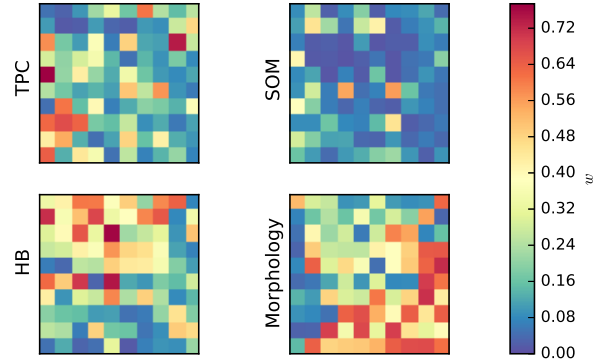


**Figure 8.** The same figure as Figure 3 but for the BMC technique applied to the four individual methods trained with the CFHTLenS data in the VVDS W1 field with  $i < 22$ .

nounced in Figure 13, where the  $P(S)$  distribution of BMC for true galaxies falls off sharply at  $P(S) \approx 0.95$ , while morphological separation and TPC techniques classify some true galaxies as stars with absolute certainty.

To identify the regions in color-color space where our BMC technique struggles to classify stars and galaxies, we present the distribution over the color-color space for sources with  $0.45 < P(S) < 0.55$  in Figure 14. Not surprisingly, these regions correspond to where there is a significant overlap between stars and galaxies in the color space. It may be possible to improve the performance of star-galaxy classification by obtaining more information through spectroscopic follow-up, manual study, or citizen science projects, or by developing a classification technique specifically designed for these regions of the color space and combining it with other techniques in a Bayesian framework.

#### 5.4 The Quality of Training Data

It is very costly in terms of telescope time to obtain a large sample spectroscopic observations down to the limiting magnitude of a photometric sample. Thus, we investigate the impact of training set quality by imposing various magnitude and  $z$  cuts to decrease the size of the training set.

In Figure. 15, we present a visual comparison between different classification techniques when various magnitude cuts are applied.

In Figure. 16, we also present the result of imposing various  $z$  cuts.

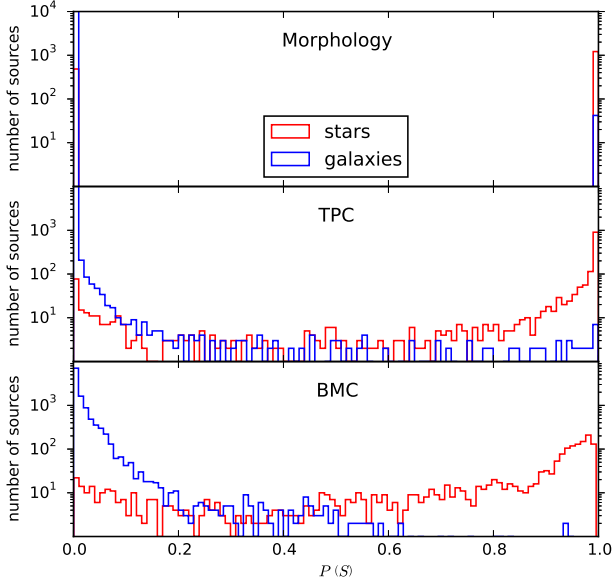


**Figure 12.** Histogram of the posterior probability that a source is a star for morphological separation (top), TPC (middle), and BMC (bottom) techniques for the entire training data (the CFHTLenS data in the DEEP2, SDSS, VIPERS, and VVDS fields as discussed in Section 5.2).

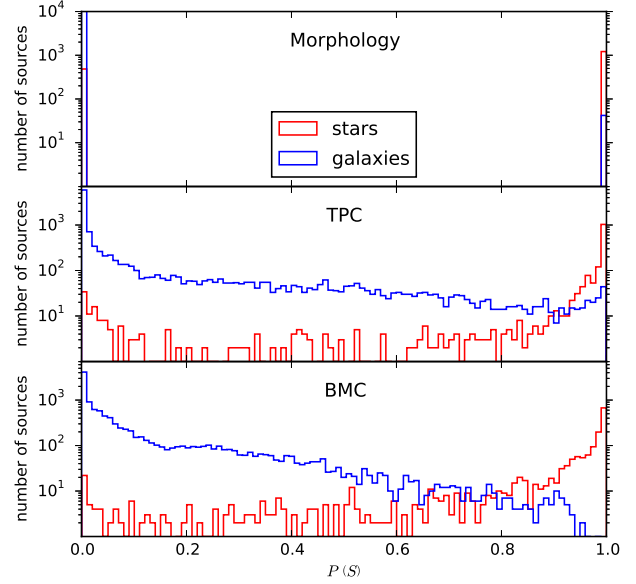


**Figure 13.** The same figures as Figure 12, but for TPC and BMC trained with poor training data (the CFHTLenS data in the VVDS field with a magnitude cut of  $i < 22$ ).

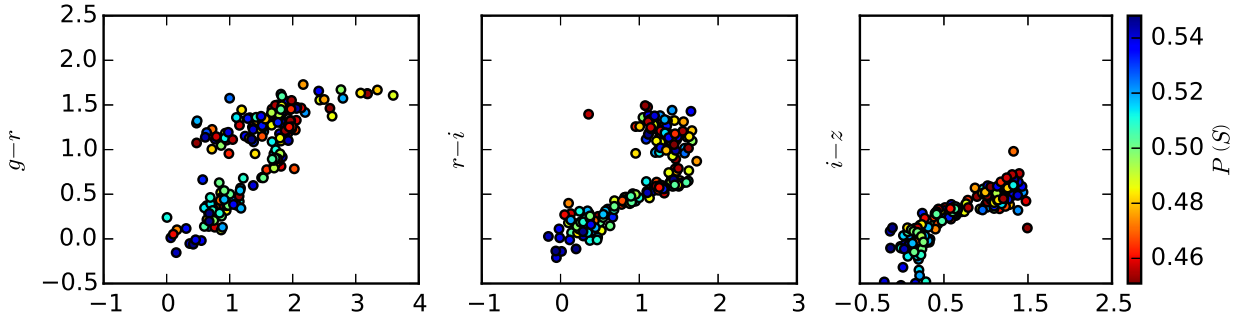


**Figure 14.** Color-color diagrams of sources with  $0.45 < P(S) < 0.55$  when the BMC technique is applied to the poor training data.

## 6 CONCLUSIONS

We have presented and analyzed a novel star-galaxy classification framework for combining classifications from the CFHTLenS project. In particular, we use four independent star-galaxy classification techniques: a morphological separation method; TPC, a supervised machine learning technique based on prediction trees and a random forest; SOMc, an unsupervised machine learning approach based on self-organizing maps and a random atlas; and HB, a hierarchical Bayesian template-fitting method that we have modified and parallelized. Both TPC and SOMc are currently available within a software package named MLZ<sup>5</sup>. Our implementation of HB and BMC, as well as IPython notebooks that were used to produce the results in this paper, are available at <https://github.com/EdwardJKim/astroclass>.

When there's wealth of training data, TPC is so good that combination techniques show no significant improvement over TPC.

Even with poor (but reasonable) training data, TPC outperforms unsupervised methods.

In a more realistic case where the training data is poor, BMC should be used.

Probabilistic classification is better. Binary classification can be transformed into a probabilistic classification when combined with other models in a Bayesian framework.

We note that Carrasco Kind & Brunner (2014a) analyzed different techniques for combining photometric redshift probability density functions (photo- $z$  PDFs), and also found that BMC is in general the best photo- $z$  PDF combination technique.

[more here](#)

<sup>5</sup> <http://lcdm.astro.illinois.edu/code/mlz.html>

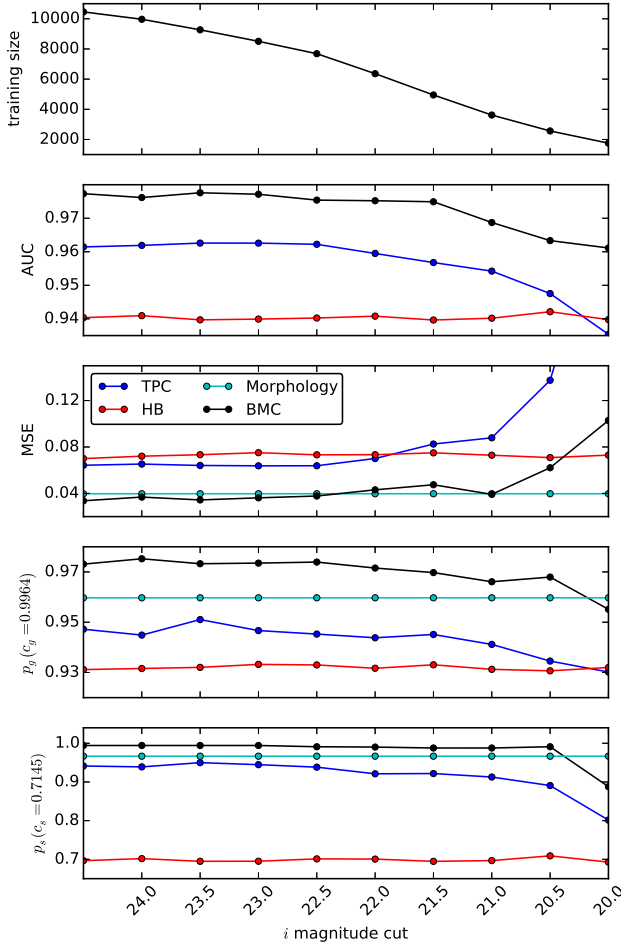


**Figure 15.** The classification performance metrics for TPC, HB, morphology, and BMC as applied to the CFHTLenS data in the VVDS field with various magnitude cuts. The top panel shows the number of sources in the training set at corresponding magnitude cuts. We show only one of the four combination methods, BMC, which has the best overall performance.

## ACKNOWLEDGEMENTS

We thank the referee for a careful reading of the manuscript and comments that improved this work. We thank Ignacio Sevilla for helpful and insightful conversations. We acknowledge support from the National Science Grant No. XXXX.

We gratefully acknowledge the use of computing resources from the Extreme Science and Engineering Discovery Environment (XSEDE), which is supported by National Science Foundation grant number XXXX.

Funding for CFHTLenS has been provided by XXXX.

## REFERENCES

- Ahn C. P. et al., 2014, *ApJS*, 211, 17  
 Ball N. M., Brunner R. J., Myers A. D., Tchong D., 2006, *ApJ*, 650, 497

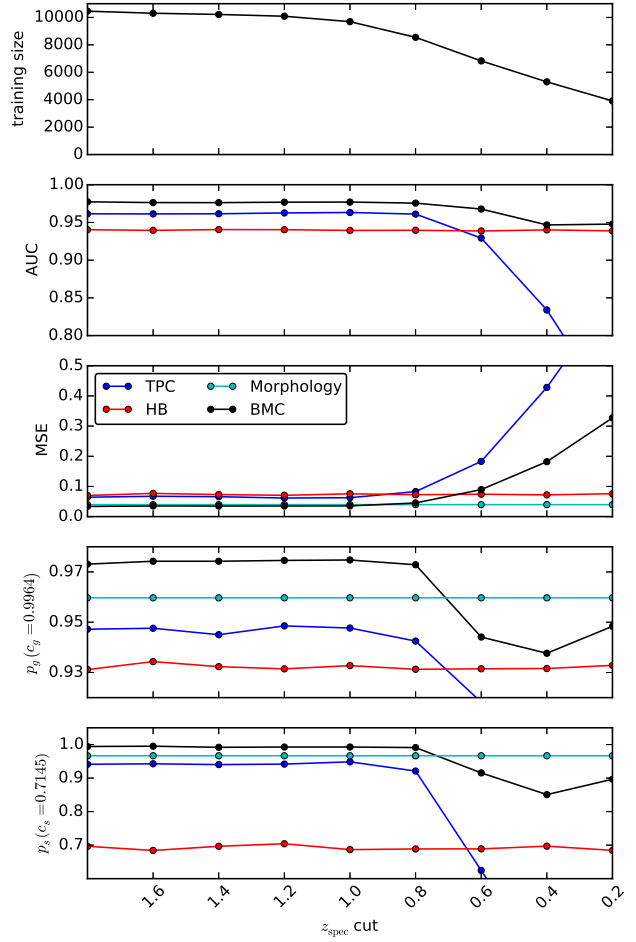


**Figure 16.** Same as Figure. 15 using  $z_{\text{spec}}$  cuts.

- Benítez N., 2000, *ApJ*, 536, 571  
 Bertin E., Arnouts S., 1996, *A&AS*, 117, 393  
 Bohlin R. C., Colina L., Finley D. S., 1995, *AJ*, 110, 1316  
 Breiman L., 1996, *Machine learning*, 24, 49  
 Breiman L., 2001, *Machine learning*, 45, 5  
 Breiman L., Friedman J., Stone C. J., Olshen R. A., 1984, *Classification and regression trees*. CRC press  
 Brier G. W., 1950, *Monthly weather review*, 78, 1  
 Carrasco Kind M., Brunner R. J., 2013, *MNRAS*, 432, 1483  
 Carrasco Kind M., Brunner R. J., 2014a, *MNRAS*, 442, 3380  
 Carrasco Kind M., Brunner R. J., 2014b, *MNRAS*, 438, 3409  
 Chabrier G., Baraffe I., Allard F., Hauschildt P., 2000, *ApJ*, 542, 464  
 Coleman G. D., Wu C.-C., Weedman D. W., 1980, *ApJS*, 43, 393  
 Davis M. et al., 2003, in *Society of Photo-Optical Instrumentation Engineers (SPIE) Conference Series*, Vol. 4834, Dis-

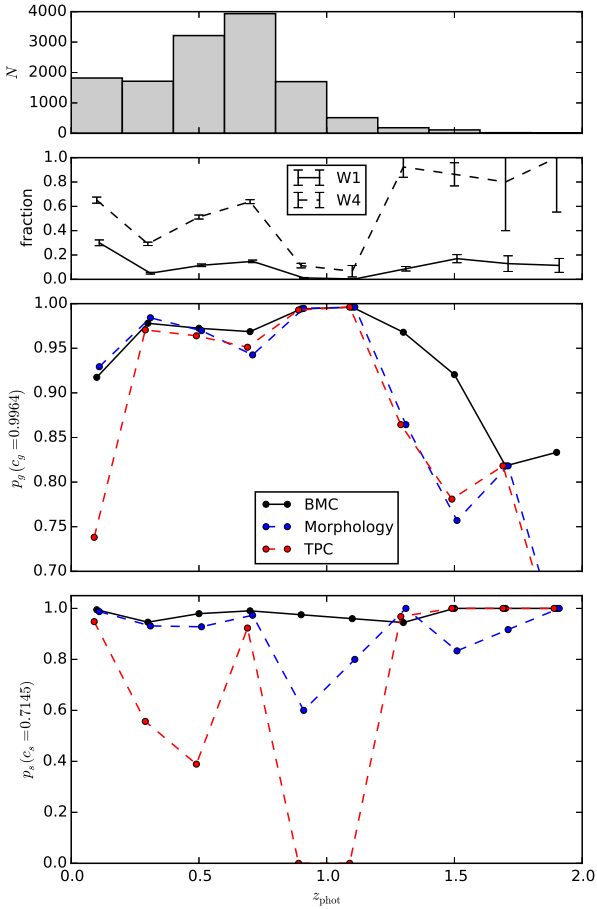


**Figure 10.** The same figures as Figure 9, but as a function of photo- $z$ .

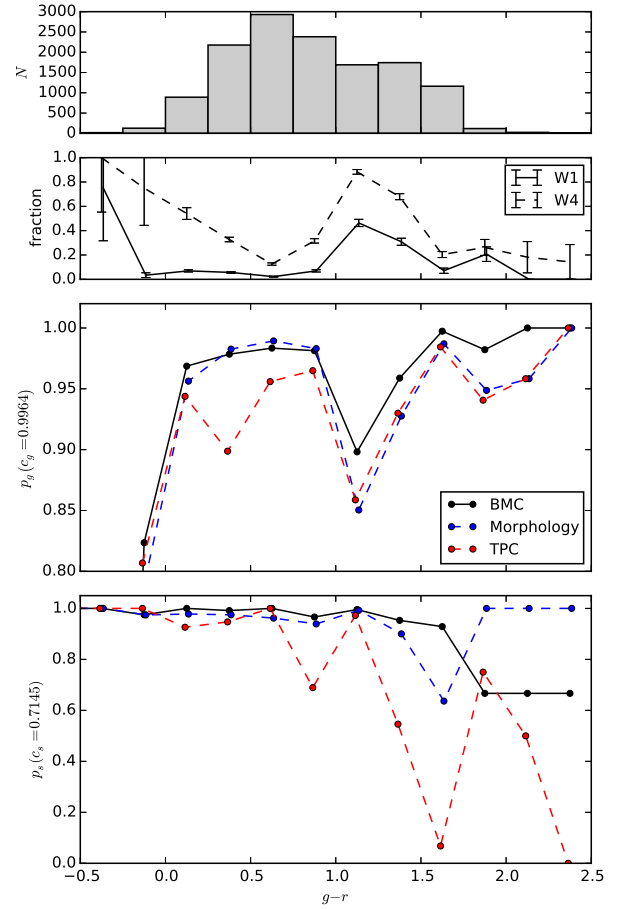


**Figure 11.** The same figure as Figure ??, but as a function of  $g-r$  color.

coveries and Research Prospects from 6- to 10-Meter-Class Telescopes II, Guhathakurta P., ed., pp. 161–172  
 Erben T. et al., 2013, MNRAS, 433, 2545  
 Fadely R., Hogg D. W., Willman B., 2012, ApJ, 760, 15  
 Foreman-Mackey D., Hogg D. W., Lang D., Goodman J., 2013, PASP, 125, 306  
 Garilli B. et al., 2014, A&A, 562, A23  
 Garilli B. et al., 2008, A&A, 486, 683  
 Górski K. M., Hivon E., Banday A. J., Wandelt B. D., Hansen F. K., Reinecke M., Bartelmann M., 2005, ApJ, 622, 759  
 Gwyn S. D., 2012, The Astronomical Journal, 143, 38  
 Henrion M., Mortlock D. J., Hand D. J., Gandy A., 2011, MNRAS, 412, 2286  
 Heymans C. et al., 2012, MNRAS, 427, 146  
 Hildebrandt H. et al., 2012, MNRAS, 421, 2355  
 Kaiser N., Squires G., Broadhurst T., 1995, ApJ, 449, 460  
 Kinney A. L., Calzetti D., Bohlin R. C., McQuade K., Storch-Bergmann T., Schmitt H. R., 1996, ApJ, 467, 38  
 Kohonen T., 1990, Proceedings of the IEEE, 78, 1464  
 Kohonen T., 2001, Self-organizing maps, Vol. 30. Springer Science & Business Media  
 Kron R. G., 1980, ApJS, 43, 305

Le Fèvre O. et al., 2005, A&A, 439, 845  
 Messier C., 1781, Connaissance des Temps for 1784, 227  
 Monteith K., Carroll J. L., Seppi K., Martinez T., 2011, in Neural Networks (IJCNN), The 2011 International Joint Conference on, IEEE, pp. 2657–2663  
 Newman J. A. et al., 2013, ApJS, 208, 5  
 Odewahn S. C., Stockwell E. B., Pennington R. L., Humphreys R. M., Zumach W. A., 1992, AJ, 103, 318  
 Pickles A. J., 1998, PASP, 110, 863  
 Robin A. C. et al., 2007, ApJS, 172, 545  
 Rokach L., 2010, Artificial Intelligence Review, 33, 1  
 Ross A. J. et al., 2011, MNRAS, 417, 1350  
 Sebok W. L., 1979, AJ, 84, 1526  
 Soumagnac M. T. et al., 2013, ArXiv e-prints  
 Suchkov A. A., Hanisch R. J., Margon B., 2005, AJ, 130, 2439  
 Swets J. A., Dawes R. M., Monahan J., 2000, Scientific American, 83  
 Ting K. M., Witten I. H., 1999, J. Artif. Intell. Res.(JAIR), 10, 271  
 Valdes F., 1982, in Society of Photo-Optical Instrumentation Engineers (SPIE) Conference Series, Vol. 331, Instrumenta-

- tion in Astronomy IV, pp. 465–472  
 Vasconcellos E. C., de Carvalho R. R., Gal R. R., LaBarbera  
 F. L., Capelato H. V., Frago Campos Velho H., Trevisan  
 M., Ruiz R. S. R., 2011, *AJ*, 141, 189  
 Weir N., Fayyad U. M., Djorgovski S., 1995, *AJ*, 109, 2401  
 Wolpert D. H., 1992, *Neural networks*, 5, 241  
 Yee H. K. C., 1991, *PASP*, 103, 396

This paper has been typeset from a  $\text{\TeX}$ / $\text{\LaTeX}$  file prepared  
 by the author.